Analyzing flow behavior of shear-thinning fluids in a planar abrupt contraction/expansion microfluidic geometry

Fatemeh Khalkhal [1,*] and Susan Muller[2,†]
[1]*Department of Mechanical Engineering, San Francisco State University, San Francisco, California 94132, USA*
[2]*Department of Chemical and Biomolecular Engineering, University of California, Berkeley, Berkeley, California 94720, USA*

(Received 3 August 2021; accepted 24 January 2022; published 16 February 2022)

We compare the flow behavior of several shear-thinning fluids of xanthan gum (XG) and polyethylene oxide (PEO) with a relatively similar shear-thinning index (∼0.34–0.50) in a microfluidic planar contraction/expansion geometry. We explore vortex formation and growth near the abrupt constriction over a wide range of Re ($0.0046 \lesssim \mathrm{Re} \lesssim 3.7$) and effective Weissenberg ($134 \leqslant \mathrm{Wi}_{\mathrm{eff}} \lesssim 9381$). An important aspect of the present study is careful rheological characterization to determine the relaxation time of aqueous solutions. From flow visualization experiments, we observed that corner vortices form in the weakly elastic aqueous solutions upstream of the constriction. In the PEO solution, a Newtonian-like behavior (with no corner vortex) was observed up to $\mathrm{Re} = 0.0067$, and the vortex length remained relatively unchanged up to much higher flow rates ($\mathrm{Re} = 0.4$). The vortex growth mechanism was observed at higher flow rates. When $\mathrm{Re} \geqslant 1$ the flow became time dependent and chaotic. In xanthan gum solutions, the initial vortex appeared at Re as low as 0.0046, and the vortex length grew by increasing the Re, and $\mathrm{Wi}_{\mathrm{eff}}$. Interestingly, at similar Re, the vortex was much longer than the one in the PEO solution and the flow remained stable over the entire range of flow rates studied. We believe fluid elasticity is central in the vortex formation and growth. The onset of vortex formation and growth shifted to lower Re and Wi by increasing the elasticity number ($\mathrm{El} = \mathrm{Wi}/\mathrm{Re}$), revealing the importance of fluid elasticity over inertia in the formation of upstream corner vortices. While chaotic flow instabilities can offer advantages in micromixing, heat, and mass transfer by employing elastic non-Newtonian fluids, instabilities have to be prevented in many other applications, including microrheometry, inkjet printing, and roll coating. Understanding the onset and mechanisms of flow instabilities can shed light on designing more efficient industrial processes and optimal products.

DOI: 10.1103/PhysRevFluids.7.023303

I. INTRODUCTION

In many high-speed industrial processes such as roll coating, inkjet printing, and fiber spinning, a complex fluid is highly stretched while passing through very small dimensions of the geometry, e.g., between the rolls of a roll-coating process or through a narrow nozzle in inkjet printing. The high extension rates induced during the process may cause flow instabilities that compromise the quality of the final products; for example, in roll coating, flow instabilities result in nonuniform film

*Corresponding author: fkhal@sfsu.edu
†muller2@berkeley.edu

thickness and wrinkles in the final film. Flow instabilities create bead structures in the woven fibers in fiber spinning, diminishing the fiber strengths [1].

Entry flows of Newtonian and non-Newtonian fluids in contraction/expansion geometries have been studied in various axisymmetric and planar geometries, among which are the work mentioned in Refs. [2–5]. As Evans and Walters [3] concluded, observations regarding the formation of vortices and flow instabilities strongly depend on the geometry and the type of fluid, and generalizations cannot be easily made.

While macroscopic abrupt contraction/expansion geometries have shed light on the entry flow of different viscoelastic fluids, many flow instabilities occur at relatively low Re and high Wi, which are typically not accessible at large scales. On the other hand, microfluidic devices provide a convenient platform to study the flow behavior of complex fluids; due to their small size, they require small quantities of samples. By designing channels with ten to a hundred micron dimensions, a small range of Re and a wide range of Wi and El can be achieved that are not accessible in macroscale. Here, we define $\mathrm{Re} = \frac{\rho \bar{V}_c D_h}{\eta(\dot{\gamma})}$, $\mathrm{Wi} = \lambda\dot{\gamma}$, and $\mathrm{El} = \frac{\mathrm{Wi}}{\mathrm{Re}}$, where ρ is the density, $\bar{V}_c$ is the average velocity in the constriction, D_h is the hydraulic diameter, $\eta(\dot{\gamma})$ is the shear rate-dependent viscosity, $\dot{\gamma}$ is the shear rate in the constriction, and λ is the relaxation time of the solutions. Apart from studying the flow kinematics and stability of various fluids, flow in narrow microfluidic constrictions can have many other applications, including the design of extensional microrheometry for weakly elastic fluids [6–10], cell separation [11,12], cell deformation under sudden and gradual extension [13], and mimicking the flow of polymeric solutions in porous media for enhanced oil recovery and groundwater remediation [14–16].

The flow of polymeric solutions in planar abrupt *microfluidic* contraction and expansions has been studied by many researchers experimentally [16–29] and numerically [7,29–33]. Below, we briefly review these efforts, highlighting those that have attempted to explain the underlying mechanisms by numerical or experimental observations.

It is customary to observe upstream vortices form near the constriction entrance in non-Newtonian (Boger, and shear-thinning) fluids where the vortex size scales with Re and Wi. The vortex size has been analyzed in a dimensionless form by dividing the vortex length (L_v) by the upstream channel width (W_u), $\chi = \frac{L_v}{W_u}$. Phase diagrams have been created to map the flow behavior of different fluids in Re-Wi space, a review of which is provided in Rodd *et al.* [17].

Some observed flow regimes in a die entry creeping flow ($\mathrm{Re} \sim 10^{-4}$–10^{-2}) of Boger fluids are identified by the experimental work of Nguyen and Boger [2] in axisymmetric geometries. They include vortex growth, asymmetric flow, rotating flow (rotation along the tube), and helical flow (rotating and translating along the tube), which appear as the flow rate increases. The authors comment that flow instabilities arise from fluid elasticity, and they initiate upstream of the contraction due to the distortion in the velocity profile. In addition, the vortex growth is a uniform function of Wi and independent of contraction ratio (CR), when CR varied between 4 and 12 and slightly dependent on CR when $\mathrm{CR} > 12$. Here and throughout this paper, CR is defined as the ratio of the diameters (in axisymmetric geometries) or widths (in planar geometries) of the upstream channel and downstream channel. Nigen and Walters [5] compared the flow behavior of Newtonian and Boger fluids of similar viscosity in axisymmetric and planar contraction geometries with $\mathrm{CR} \sim 2$–40. They observed that the vortex formation and growth, and the pressure drop in the constriction, are much more pronounced in axisymmetric geometries.

A so-called vortex enhancement mechanism is usually observed in planar geometries, where a salient corner vortex forms and its size scales with flow rate. Evans and Walters [3] compared the behavior of Boger and shear-thinning fluids in planar and axisymmetric contraction geometries and concluded that shear-thinning must be present in all contraction ratios (including 4:1, 16:1, and 80:1) to observe significant salient corner vortex and vortex growth. The vortex enhancement is truncated at a critical Re when both elasticity and inertia become important and is often followed by the formation of diverging flow patterns. In a divergent flow, the streamlines locally diverge from the centerline upstream of the constriction and converge as they enter the constriction [17]. This phenomenon is usually observed in shear-thinning fluids but has also been reported in Boger fluids

at relatively low Re (Re ~ 0.04 in axisymmetric contractions [34]). The emergence of divergent flow patterns has been observed experimentally in planar contractions by Rodd *et al.* [17] and by many others numerically, including Oliveira and Pinho [35] and Alves *et al.* [33]; more details about divergent flow can be found in the work of Cable and Boger [36]. Using numerical methods in planar geometries with rounded corners (as opposed to sharp corners), Alves *et al.* [33] suggested that both inertia and (or) shear thinning are not required for divergent flow to appear. At the same time, Rodd *et al.* [18] experimentally showed the importance of El in the formation of diverging flow patterns in entry flow of weakly elastic polymeric solutions in microfluidic planar contraction and expansions; diverging flow patterns do not necessarily appear at the onset of viscoelastic Mach number (Ma) > 1, where Ma $= \sqrt{\mathrm{Re\,Wi}}$, but El has to be relatively large (e.g., El ~ 68 in their case) for the emergence of diverging flow. This can also explain the absence of diverging streamlines as an indication for viscoelastic effects in entry flow of fluids with low elasticity numbers even when Ma > 1.

Depending on the elasticity of solutions, viscoelastic entry flows may become unstable in moderate ranges of Re and Wi [17]. The instability can be manifested by an unstable salient corner vortex or the formation of Goertler-like and lip vortices [37,38], which are typically observed in shear-thinning fluids in devices with 4:1 contraction ratios and aspect ratios (we define the aspect ratio to be h/w_c, where h is the depth of the device in the neutral direction and w_c is the width of the channel in the constriction) greater than 20.

In planar geometries, Evans and Walters [4] confirmed a lip-vortex mechanism is responsible for vortex enhancement in all contraction ratios, which can only be experimentally observed over a limited range of flow rates and in some specific polymer concentrations. Moreover, they reported that wall imperfections in the reentrant geometry could significantly affect the shape, size, and symmetry of the corner vortex in Boger fluids, but it hardly affects the behavior of shear-thinning fluids in a similar geometry. These observations were later confirmed by the numerical work of Alves *et al.* [31,32] in a Boger (Oldroyd-B) and a viscoelastic shear-thinning [Phan-Thien–Tanner (PTT)] fluid in microfluidic planar abrupt contractions, with a solvent viscosity ratio β ($\beta = \frac{\eta_s}{\eta_s+\eta_p}$, where η_s and η_p are the solvent viscosity and zero-shear polymer viscosity, respectively) of $1/9$. They showed that vortices formed upstream of the constriction and the corner vortex length scaled logarithmically with the De number, (where De is defined as De $= \frac{\lambda U_2}{H_2}$, and λ is the relaxation time, U_2 is the cross-sectional average velocity in the smaller channel, and H_2 is the half height of the smaller outflow channel) for a linear PTT fluid and decreased linearly with De for an Oldroyd-B fluid at CR $\sim 4:1$. When CR > 4, Alves *et al.* [32] confirmed the presence of a lip vortex and the evidence of lip-vortex enhancement mechanism in the creeping flow of PTT fluids. In addition, the dimensionless corner vortex length was shown to scale logarithmically with De/CR, whereas the lip vortex scaled with De. Moreover, at an onset De/CR ~ 1.0, the fingering of the corner vortex towards the reentrant vortex was completed, and the vortex began to grow from a concave to a convex shape.

In axisymmetric geometries, Rothstein and McKinley [39] explained the vortex growth dynamics to be a consequence of two competing effects, including the shear rate at the upstream walls of the contraction where $\dot{\gamma} \propto 1/\mathrm{CR}^3$ and the accumulated strain along the flow centerline $\varepsilon \propto \ln \mathrm{CR}$. They suggested that at small enough contraction ratios, very low extension rates are present, leading to lip-vortex formation. By increasing the De (or contraction ratio), the extensional stresses increase and dominate normal stress differences arising from shear; this leads to the formation of a corner vortex and displacement of the lip vortex. They concluded that transitions in vortex growth are associated with extensional properties of viscoelastic fluids and affect equilibrium conformations of the polymer chains. The chain conformations are influenced by solvent quality or stiffness of the polymer backbone, as suggested in Refs. [40–42]. The importance of locally increased strain rates and fluid extensional rheology in the dynamics of vortex formation and growth has been further emphasized by three-dimensional (3D) flow visualizations in a recent work in Ref. [28]. Rodd *et al.* [43] experimentally showed that the upstream vortex formation is a consequence of stretching dynamics in the constriction and the downstream relaxation in the expansion is

equivalently important. They supported this argument by analyzing the effect of constriction length on upstream vortex formation and stability in a planar contraction/expansion microfluidic device. Their observations revealed that an entirely stable symmetric upstream vortex could be converted into a chaotic asymmetric vortex by increasing the constriction length. At the same time, by increasing the elasticity number (e.g., via increasing the solvent viscosity), the upstream flow instabilities can be controlled to some extent. A recent study by Raihan *et al.* [44] also considered the effect of constriction length on both contraction and expansion flows of a constant viscosity, viscoelastic polyethylene oxide (PEO) solution, a shear thinning xanthan gum solution, and a shear-thinning, viscoelastic polyacrylamide solution, and found that only the PEO solution showed constriction length-dependent instabilities for the contraction flow.

Sousa *et al.* [23] investigated the flow of Newtonian and shear-thinning fluids in a square-square microfluidic abrupt contraction/expansion flow over several contraction ratios (i.e., CR $\sim$ 2.4, 4, 8, and 12) experimentally and numerically. For the shear-thinning fluid, a corner vortex was observed independent of the contraction ratio. They observed that by increasing the flow elasticity, the vortex size strongly increased while still at low Re until an elastic instability emerged; the flow became time dependent at De $\approx$ 200, 300, 70, and 450 for CR $=$ 2.4, 4, 8, and 12, respectively. Lanzaro and Yuan [24] investigated the effects of contraction ratio on nonlinear dynamics of semidilute, highly polydisperse polyacrylamide (PAAm) solutions in microfluidic contraction/expansion geometries. They reported that the stability of the nonlinear flow structures could be tuned by El and that the geometry (contraction ratio and aspect ratio), Wi and Re, and molecular weight distribution of polymers affect the viscoelastic flow phenomena. A series of different microfluidic geometries with strong extensional components have been studied experimentally by Galindo-Rosales *et al.* [9]. Depending on the geometry, Wi and Re, they observed different types of flow transitions, including transition from a steady symmetric to steady asymmetric and unsteady flows and a direct transition from steady symmetric to unsteady flows.

Haward *et al.* [21] investigated flow instabilities of polystyrene (PS) solutions in a planar 8:1:8 geometry in a wide range of Re ($0.07 < \mathrm{Re} < 11.2$), Wi ($8.7 < \mathrm{Wi} < 1562$) and elasticity numbers ($31 < \mathrm{El} < 295$). They reported flow transitions spanning between Newtonian-like flow (i.e., stable converging streamlines near the constriction) to unstable flow at the critical Wi $=$ 150 and from unstable flow to vortex growth in the upstream salient corners at the critical Wi $=$ 400. Transitions between the flow regimes scaled with Wi, independent of El, revealing the importance of elastic forces compared to inertial effects in all the fluids they studied. By combining birefringence analysis with flow measurements, Haward *et al.* estimated the macromolecular strain values in the microchannel constriction. For the Newtonian-like flow regime (Wi $\leqslant$ 150), this strain value was reported to be zero but increased with the emergence of the unstable flow and reached a plateau value at the onset of vortex growth (Wi $\geqslant$ 400).

Despite extensive work in the entry flow of non-Newtonian fluids in abrupt contraction/expansion geometries, there are unexplored features and unexplained mechanisms. For example, the mechanism of flow instabilities and time-dependent behavior is not well known yet, in part because characterizing some fluid properties, such as the relaxation time, have created discrepancies that make comparisons between different experiments and simulations challenging. In addition, the type of fluid, contraction ratio [45], and aspect ratio [7] strongly affect the flow behaviors. Moreover, the competition of shear and extension near the flow reentrance presents additional complications to the flow behavior that cannot be easily explored in a rheometer. Therefore, it is worth testing more fluids in various geometries and over a broader region in Wi-Re space both to gain additional insight and to design strategies for more efficient industrial processes such as enhanced oil recovery and extensional microrheometry.

In the present study, we compare the flow behavior of several shear-thinning fluids of xanthan gum (XG) and polyethylene oxide (PEO) in a planar contraction/expansion geometry that is symmetric in the flow direction (fore-aft) and symmetric about the midplane of the depth and asymmetric with respect to the "contraction" direction (Fig. 1). The solutions are prepared to have a relatively similar shear thining index ($\sim$0.34–0.50). We explore vortex formation and growth near the abrupt

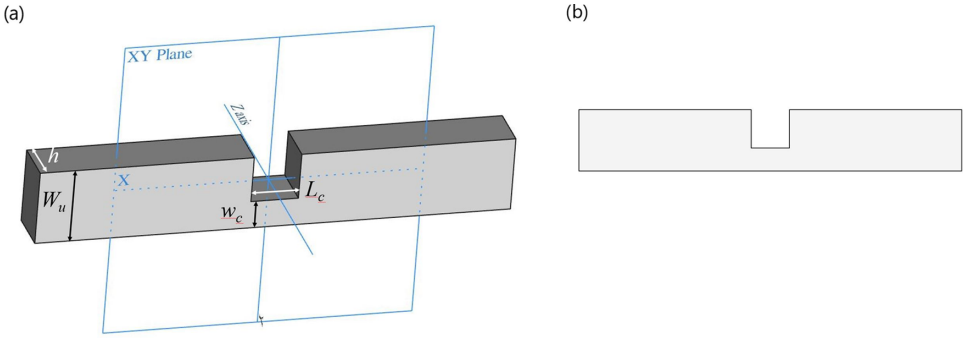

FIG. 1. Schematic of the device with a nominal contraction ratio of 4. (a) 3D view, (b) side view in XY plane. The device dimensions include $W_u = 460$–$475\,\mu$m, $w_c = 101.6$–$106.7\,\mu$m, $L_c = 418\,\mu$m, $h = 215.6$–$219\,\mu$m. The flow is from left to right. The device is about 13 mm long on each side of the constriction. The videos were captured in the middle of the channels at $z = 0$.

constriction at different flow rates in this geometry. We explore flow behavior for shear-thinning fluids over a broad range of Re ($0.0046 \lesssim \mathrm{Re} \lesssim 3.7$) and Wi ($134 \leqslant \mathrm{Wi} \lesssim 9381$). An important aspect of the present study is careful rheological characterization to determine the relaxation time of aqueous solutions in the absence of the Capillary Breakup (CaBER) instrument. Moreover, by preparing solutions with similar shear-thinning indices, we can examine the importance of other parameters, such as the interplay between inertia and elasticity in vortex formation and flow instabilities.

Below, we present the experimental procedures, including microfluidic device fabrication, sample preparation, rheological characterization, and flow visualization methods, followed by a discussion and further analysis of rheological results and flow visualization observations. A comparison of vortex growth behavior is made between the aqueous fluids over a wide range of Re and Wi, followed by more general conclusions.

II. EXPERIMENTAL PROCEDURE

A. Microfluidic device fabrication

Microfluidic devices were fabricated using a low-cost, fast prototyping technique reported in Ref. [46]. The schematic of the device with a nominal contraction ratio of 4:1 and a nominal aspect ratio of 2 is shown in Fig. 1. A significant difference between our geometry and the benchmark planar contraction/expansion geometries is that it is symmetric about the obstacle in the y and z directions but not in the x direction. The lower wall in this geometry creates a high shear stress boundary to flow instead of the zero shear stress boundary in benchmark planar geometries due to their symmetry in the x, y, and z directions.

Initially, a dry film photoresist of the Riston GoldMaster (GM) 100 series (DuPont) was laminated on a steel wafer (Stainless Supply) to make a master. The lamination was performed in an Akiles Prolam-Ultra laminator at 120 °C. The Riston Goldmaster is available in three nominal thicknesses of 50, 75, and 100 μm. We were able to make masters of various thicknesses (h in Fig. 1) by employing different combinations of film thicknesses. The microchannels were designed in AutoCAD and printed on laser-plotted polyester-based film photomasks in 40 640 DPI (equivalent to 8 μm resolution) by Fineline Imaging (Colorado Springs, CO). The mask was lined up with the master on an OAI Series 200 lithographic mask aligner in vacuum contact mode with a 350-W UV lamp ($\lambda \sim 360$–440 nm) and exposed for a calculated time. The exposed masters were then developed in a 10 g/l potassium carbonate solution while constantly agitated on a Bellco orbital shaker at 67 rpm to remove the unexposed film. Finally, the developed masters were rinsed with de-ionized water and dried with an air gun.

The microfluidic devices were produced from the masters via casting and curing polydimethylsiloxane (PDMS) and bonding the PDMS devices to glass coverslips. A Sylgard® 184 silicone elastomer kit (Dow Corning) with a 10:1 base to curing agent ratio was thoroughly mixed and degassed in vacuum for 1 h at room temperature. The degassed PDMS was then poured over the master and degassed again for another 30–60 min in a vacuum. After removing all air bubbles, the PDMS was cured at 60 °C for 4 h in a vacuum oven. Inlet and outlet holes were punched in the PDMS devices using a 22-G blunt tip needle (McMaster-Carr). Before bonding the cured PDMS devices onto the glass slides, scotch tape was attached to the channel surfaces on PDMS to remove any potential debris. PDMS devices were then bonded to glass coverslips (Fisherbrand, cover glass No. 1) using a handheld laboratory corona discharger (BD-20AC, Electro-Technic Products). Flexible Tygon tubing with 1/16-in. inner diameter was attached to the through holes of the reservoirs. Here, 2.5-mL gastight glass syringes (Hamilton) were threaded with a 22-G plastic dispensing tip (McMaster-Carr) attached to the tubing. The flow rate was controlled with a Harvard Apparatus PHD 2000 syringe pump.

The actual depth of the channels was measured on PDMS replicas before bonding them to glass slides using an optical profilometer (Solarius Development LaserScan) and the index of refraction of PDMS was set to 1.40. This strategy was employed since the exact thickness of the masters could not be directly measured due to the unknown refractive index of the UV exposed Riston photoresist. More details about the fabrication process can be found in Ref. [46]. A schematic of the device is shown in Fig. 1, with the actual dimensions as the following: the upstream channel's width, $W_u = 460$–475 μm, the constriction width, $w_c = 101.6$–106.7 μm, the constriction length, $L_c = 418$ μm, and the depth, $h = 215.6$–219 μm; the actual aspect ratios (h/w_c) and contraction ratios were 2.16 and 4.675 in the devices used for xanthan gum solutions and were 2.02 and 4.31 in the devices used for the PEO solutions, respectively. The upstream and downstream channels were roughly 13 mm in length on each side of the constriction.

Due to the small size of the obstacles, i.e., several hundred μm in length (L_c) by a few hundred μm in width (w_c), one may need to apply some extra pressure when bonding PDMS to glass. Applying an uneven extra force may result in uneven pressure distribution on one side of the device and, consequently, tilt the obstacle as it bonds to the glass. The nonuniform attachment of obstacle walls to glass can result in a nonrectangular (e.g., trapezoidal) flow cross section under the obstacle that can change the flow pattern and velocity field, shear stress, and pressure distribution near the obstacle. The width of the obstacle (w_c) was examined and measured at different depths while the device was filled with water or isopropyl alcohol. In all cases, the width of the obstacle remained uniform.

The exact dimensions of devices may slightly change from one device to another, therefore the more accurate CR is reported for each device in the figure captions. In all cases, the channel depths were around the nominal value of 200 μm. Also, due to the relatively short length of the constriction, we expect the flow to be far from fully developed in the constriction area, which should be responsible for interesting phenomenon upstream of the constriction.

B. Sample preparation

Aqueous solutions of polyethylene oxide POLYOX 301 (PEO) with a molecular weight of 4×10^6 g/mol and xanthan gum (KELTROL, CP Kelco) with a molecular weight of 2 MDa were used in this study. Xanthan gum (XG) is a water-soluble, anionic polysaccharide produced by the bacterium *Xanthomonas campestris* [47]. It has been used in food and personal care products to provide stability, suspension, texture, pouring characteristics, and cling; it is also an excellent binder in regular and specialty toothpaste, including antitartar and sensitive teeth toothpaste. Other important industrial applications of xanthan gum include long-term suspension and emulsion stability in alkaline, acid, and salt solutions, temperature resistance and pseudoplasticity, and shear thinning (particularly useful in drilling, production, hydraulic fracturing, and enhanced oil recovery) [48]. In the absence of any added ions, the aqueous xanthan gum molecules are fully extended due to the

electrostatic repulsion of the negatively charged sidechains [49]. PEO is a nonionic water-soluble polymer that offers many different properties, including lubricity, binding, water retention, and thickening in various applications, including aqueous drag reduction and drift control, personal care products [50], to name a few.

Aqueous solutions of xanthan gum and PEO were prepared at various concentrations spanning from 0.1 to 1.0 wt%. Glycerol was added to 0.1 wt% xanthan gum solutions to increase viscosity at a maximum concentration of 56 wt% (equivalent to 50 vol%). The solutions were stirred on a stirring plate at the lowest possible rate until the polymer powder was dissolved within a few hours. PEO solutions with relatively higher concentrations (e.g., ∼1.0 wt%) took much longer (∼1–2 days) to dissolve. We found the following preparation approach to be very efficient for PEO solutions. A 1-in. magnetic stirring bar was placed in an 80-mL VWR wide-mouth glass jar containing ∼40 mL of de-ionized water. The weighed PEO powder (e.g., 0.6 g for a 1.0 wt% solution) was then uniformly spread on the water surface to avoid any coagulation of the powder, which can significantly extend the dissolution time. Then, 20 mL of water was carefully added to the powder using a spray bottle. It is better to point the top of the spray bottle on the jar walls to ensure air bubbles are not introduced to the solution. The weight of the whole container was measured after closing the top. The container was then placed on a stirring plate, and the solution was mixed at the lowest possible rate for a couple of days until the PEO was entirely dissolved. The container's weight was measured after the powder was entirely dissolved and compared with its initial weight to ensure the absence of evaporation. In case of any evaporation, de-ionized water was added to match the original weight of the whole container before mixing.

The radius of gyration (R_g) and the extensibility parameter (L^2) have been estimated for our solutions which are comparable to literature values. Whitcomb *et al.* [51] reported a hydrodynamic length of 1.5 μm and an extended length of 8.7 μm for xanthan gum with $M_w \sim 7.6 \times 10^6$. Milas and Rinaudo [52] estimated the mass per unit length of xanthan gum with $M_w \sim 6.5$–7.0×10^6, to be $M_L = 100$ g/A, and the contour length, L_c to be $L_c = \frac{M_w}{M_L}$ or simply 65 000–70 000 A (equivalent to 6.5–7.0 μm). In our studies, $M_w \sim 2$ MDa for xanthan gum (KELTROL, CP Kelco); using $L_c = \frac{M_w}{M_L}$, we estimate L_c to be about 2.0 μm. Assuming $R_g^2 \sim M_w$ for random coils [53], the radius of gyration can be estimated to be $R_g \sim 141$ nm. The extensibility parameter is then calculated using $L^2 = (\frac{L_c}{\sqrt{6}R_g})^2$ as indicated in Burshtein *et al.* [54] to be 33.5 for xanthan gum. For the PEO with $M_w \sim 4 \times 10^6$, we use R_g and L^2 to be about 152 nm and 5000 [54]. The estimated values for the extensibility parameter show that PEO molecules should be a lot more extensible ($L^2 \sim 5000$) and therefore flexible in comparison with xanthan gum ($L^2 \sim 33.5$).

The overlap concentration was estimated to be 0.0282 wt% (or simply 282 ppm) for xanthan gum using $c^* = \frac{3\,M_w}{4\,N_A \pi R_g^3}$ [55], where $R_g = 141$ nm and $M_w \sim 2$ MDa; the estimated overlap concentration is similar to 254 ppm reported by Raihan *et al.* [44] for a 2-MDa xanthan gum. For PEO with $M_w \sim 4 \times 10^6$ Da, we use $c^* = 0.045$ wt% or (450 ppm).

C. Rheological characterization

A Bohlin C-VOR (MALVERN Instruments) rheometer with two geometries, parallel plate (PP40) and cone and plate (CP40, with 4° angle), was used to characterize the rheological properties of the solutions at room temperature (i.e., 25 °C). Initially, the shear viscosity of xanthan gum solutions of various concentrations was measured with both geometries (gap size: 0.8–2.0 mm for PP40 and 50 μm for CP40) to ensure the lack of any wall slip. The steady shear results were identical at each concentration using PP40 and CP40. First normal stress coefficients ψ_1 could not be measured experimentally for various solutions due to the very low normal force levels, and the data were too noisy to be reported here.

Different rheological characterizations, including steady shear, creep, and small amplitude oscillatory shear (SAOS) measurements, were performed. More details about these experiments and curve fitting of experimental results with different models are explained in Sec. III.

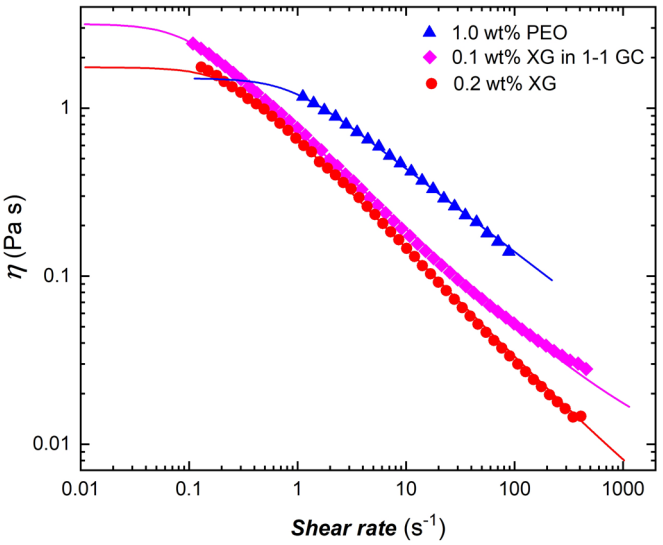

FIG. 2. Steady shear viscosity of aqueous solutions. The data points show the experimental measurements and the lines represent the best fits with the Carreau model.

D. Flow visualizations

Flow visualization experiments were performed using fluorescence microscopy. A Leica DMIRE2 inverted microscope was used with an external light source (Leica EL6000). A dual-band excitation/emission filter (Chroma 51004v2, 460–500/510–560 nm) was shown to be suitable for our system. Here, 10× (Olympus) objectives were employed for flow visualization experiments. Images and videos were taken by using a monochromatic Photometrics Cascade 512b charge-coupled-device (CCD) camera. The aqueous solutions were seeded with 0.005–0.02 vol/vol % of 1-μm fluorescent polystyrene spheres (Fluoro-MaxTM green, Thermo Scientific). Then, 88.7 and 79.2 mg sodium chloride was added per gram of 0.2 wt% XG solution and 1.0 wt% PEO solution, respectively, to match the density of the aqueous solutions to the fluorescent particles and ensure solutions remain neutrally buoyant. It was observed that the vortex in xanthan gum solutions reached its maximum length shortly after the flow rate was set, while for PEO solutions it took a few minutes. So, each flow rate was maintained for at least 10 min before videos were taken. It is worth mentioning that by using glass syringes instead of plastic ones, flow vibrations induced by the syringe pump were minimized. In order to remove trapped air bubbles from our devices, each device was initially flushed with a high concentration isopropyl alcohol (IPA) solution followed by rinsing with water for 5–10 min before we ran the polymer solutions through each device. This procedure was shown to be promising in cleaning the devices from any potential debris or air bubbles.

III. RESULTS AND DISCUSSION

A. Rheological characterization

Steady shear measurements were performed from high to low and then low to high shear rates, and it was observed that the data overlapped to a great extent. The average of the two experimentally measured data sets is reported in Fig. 2 and compared with the Careau model given in Eq. (1). From Fig. 2, it can be observed that all solutions demonstrate significant shear-thinning behavior and were well fitted with the Carreau model. The fitting parameters along with the overlap concentration c^* are summarized in Table I. The Carreau model has four parameters, including η_0 and η_∞ which are the zero shear and high shear viscosities, respectively, $\dot{\gamma}_c$ is the onset of shear thinning and one of

TABLE I. Parameters of curve fitting for Carreau model (1) in Fig. 2.

Solution	c^* (ppm)	η_0 (Pa s)	η_∞ (Pa s)	n	$\dot{\gamma}_c$ (s^{-1})
0.1 wt% XG in 1-1 GC		3.16	0.006	0.40	0.089
0.2 wt% XG	282	1.75	0.001	0.34	0.23
1.0 wt% PEO	450 [54]	1.50	0.001	0.50	0.83

the fitting parameters, and n is the shear-thinning index ($n = 1$ for Newtonian fluids and $0 < n < 1$ for shear-thinning fluids),

$$\eta(\dot{\gamma}) = \eta_\infty + (\eta_0 - \eta_\infty)\left[1 + \left(\frac{\dot{\gamma}}{\dot{\gamma}_c}\right)^2\right]^{\frac{n-1}{2}}. \tag{1}$$

The viscosity of the aqueous solvent with 50 vol% (∼56 wt%) glycerol (hereafter referred to as 1-1 GC) was measured to be constant and equal to 0.006 Pa s; therefore, for curve fitting purposes, η_∞ was set to 0.006 Pa s in 0.1 wt% XG in 1-1 GC solution and 0.001 Pa s, equivalent to the viscosity of water, in other solutions. From the results reported in Table I, it is evident that all solutions show a shear-thinning behavior with 0.2 wt% XG solution slightly more shear thinning and 1.0 wt% PEO moderately shear thinning with $n = 0.50$.

The shear-thinning index reported in Table I is consistent with literature values. At relatively high concentrations (⩾1 wt%), xanthan gum solutions can be highly shear thinning ($n \sim 0.12$–0.14), which facilitates their processing in food, cosmetic, and pharmaceutical industries [56]. Other reported values for the shear-thinning index of xanthan gum solutions span from 0.54 to 0.71 for 0.03–0.2 wt% aqueous solutions, respectively [57], 0.97 for 0.01 wt% solution, and 0.23 for 0.5 wt% solution using power-law correlations [58]. In a recent work by Raihan *et al.* [44] the shear rheology of a 2000-ppm aqueous XG solution along with the best fit with the Carreau model was reported; the fitting parameters were quite consistent with the ones reported in Table I, with $n = 0.33$, $\eta_0 = 1740$ mPa s, $\eta_\infty = 1.8$ mPa s, and a time constant (equivalent to $1/\dot{\gamma}_c$ in Table I) of 6.6 s. For 3390 ppm (or 0.34 wt%) PEO with 2×10^6 g/mol molecular weight in a solvent containing 60 wt% de-ionized (DI) water and 40 wt% PEG (with $M_w = 8000$ g/mol), the shear-thinning index was reported to be ∼0.889 [59] and ∼0.878 [60], respectively.

We used dimensionless numbers, the Weissenberg (Wi), the Reynolds number (Re), and the elasticity number (El) to analyze the results. Re represents the ratio of inertial to viscous forces and is defined in (2). Wi denotes the ratio of elastic forces to viscous forces and is defined in (3). Wi is the product of the fluid relaxation time and a characteristic rate of deformation, and therefore has been widely used as a suitable dimensionless number to analyze the nonlinear rheological effects in the entry flow of non-Newtonian fluids. Here, we use $\mathrm{Wi}_{\mathrm{eff}}$ defined in (4), which is scaled with the solvent to total viscosity ratio, β (where $\beta = \frac{\eta_s}{\eta_s+\eta_0}$ with η_s as the solvent visocity and η_0, as the zero shear visocsity from Table I). By using $\mathrm{Wi}_{\mathrm{eff}}$, we can account for the solvent contibution to the shear stress τ_{xy} as suggested in Refs. [54,29],

$$\mathrm{Re} = \frac{\rho \bar{V}_c D_h}{\eta(\dot{\gamma})} = \frac{2\rho Q}{(h + w_c)\eta(\dot{\gamma})}, \tag{2}$$

$$\mathrm{Wi} = \lambda\dot{\gamma} = \frac{\lambda Q}{h w_c^2/2}, \tag{3}$$

$$\mathrm{Wi}_{\mathrm{eff}} = \mathrm{Wi}\,(1-\beta) = \lambda\dot{\gamma}(1-\beta), \tag{4}$$

$$\mathrm{El} = \frac{\mathrm{Wi}_{\mathrm{eff}}}{\mathrm{Re}} = \frac{\lambda\,(1-\beta)\,\eta(\dot{\gamma})\,(h + w_c)}{\rho h w_c^2} = \frac{2\lambda\,(1-\beta)\,\eta(\dot{\gamma})}{\rho}\frac{1}{w_c D_h}. \tag{5}$$

In the above equations, ρ is the density, $\bar{V}_c$ is the average velocity in the constriction, Q is the volumetric flow rate, h is the channel depth, w_c is the width of the constriction (defined in Fig. 1), D_h is the hydraulic diameter, $\eta(\dot{\gamma})$ is the shear rate-dependent viscosity extrapolated using the Carreau model and the curve fitting parameters, and λ is the relaxation time of the solutions. By using the mean velocity and device dimensions in the constriction (i.e., $\bar{V}_c$ and w_c), the highest value of Re in the device was estimated at each flow rate. The range of shear rates corresponding to the flow rates in flow visualization experiments spans from 17 to 12 000 s^{-1} for 0.1 wt% XG in 1-1-GC, 74–673 s^{-1} for 0.2 wt% XG, and 113–3395 s^{-1} for PEO solutions.

Elasticity number declares the importance of elastic forces to inertial forces and is defined in (5). As shown in (5), El depends on fluid properties [i.e., λ, ρ, β, and $\eta(\dot{\gamma})$] and the characteristic lengths of the device (i.e., D_h and w_c).

To estimate Wi, we need to estimate the relaxation time of the solutions. The Capillary Breakup Extensional Rheometer (CaBER) is a well-known instrument to measure the relaxation time, time to break up, and extensional viscosity of dilute polymer solutions. In this technique, the material goes through a step uniaxial extension with a set value until it necks and finally breaks due to the action of capillary forces. Even though CaBER has been shown to help estimate the relaxation time of dilute polymer solutions, it has some drawbacks. For example, Haward *et al.* [61] suggested that hydrophobic molecules can migrate to the material-air interface, affecting the extensional properties and time to breakup by changing the interfacial rheology. In addition, it is nearly impossible to impose a controlled deformation rate on a fluid using CaBER.

In the absence of CaBER, we used creep experiments and small amplitude oscillatory shear measurements to estimate the relaxation time of our polymer solutions. Creep experiments were performed at several different constant shear stresses ranging between 0.01 and 1.0 Pa, and creep compliance (J) was measured. The results were then compared with theoretical predictions using the differential form of the Maxwell model as the constitutive equation in (6) with the boundary conditions expressed in (7),

$$\tau + \lambda \frac{\partial \tau}{\partial t} = -\eta_0 \dot{\gamma} \rightarrow \tau_{12} + \lambda \frac{\partial \tau_{12}}{\partial t} = -\eta_0 \dot{\gamma}_{12}, \tag{6}$$

$$\tau_{12} = \lim_{\varepsilon \to 0} \begin{cases} 0, & t \leqslant 0, \\ \frac{\tau_0 t}{\varepsilon}, & 0 < t \leqslant \varepsilon, \\ \tau_0, & t > \varepsilon, \end{cases} \tag{7}$$

where $\boldsymbol{\tau}$ is the shear stress, t is the time, and τ_0 is constant shear stress imposed at $t = 0$ that continues for a time period of t, η_0 is the zero shear viscosity, and λ is the relaxation time. $\dot{\gamma}$ is the strain rate and can be analytically calculated using the constitutive Eq. (6). Assuming, it would take an ε amount of time for the stress to reach its final value, the shear stress increases at a rate of $\frac{\partial \tau_{12}}{\partial t} = \frac{\tau_0}{\varepsilon}$ until the final value τ_0 is obtained. Accordingly, the shear rate $\dot{\gamma}_{12}$, and therefore the strain γ_{12}, can be analytically calculated as follows:

$$\dot{\gamma}_{12} = \begin{cases} 0, & t < 0, \\ -\frac{\tau_0}{\eta_0 \varepsilon}(t + \lambda), & 0 < t \leqslant \varepsilon, \\ \frac{-\tau_0}{\eta_0}, & t > \varepsilon, \end{cases} \tag{8}$$

$$\begin{aligned} \gamma_{12}(0,t) = \int_0^t \dot{\gamma}_{12}(t')\, dt' &= \lim_{\varepsilon \to 0} \left\{ \int_0^{\varepsilon} \dot{\gamma}_{12}(t')\, dt' + \int_{\varepsilon}^{t} \dot{\gamma}_{12}(t')\, dt' \right\} \\ &= \lim_{\varepsilon \to 0} \left\{ \int_0^{\varepsilon} \frac{-\tau_0}{\eta_0 \varepsilon}(t' + \lambda)\, dt' + \int_{\varepsilon}^{t} \frac{-\tau_0}{\eta_0}\, dt' \right\} \\ &= \frac{-\tau_0}{\eta_0} \lim_{\varepsilon \to 0} \left\{ \frac{1}{\varepsilon} \left(\frac{t'^2}{2} + \lambda t' \right)_0^{\varepsilon} + (t')_{\varepsilon}^{t} \right\} = \frac{-\tau_0}{\eta_0}(t + \lambda). \end{aligned} \tag{9}$$

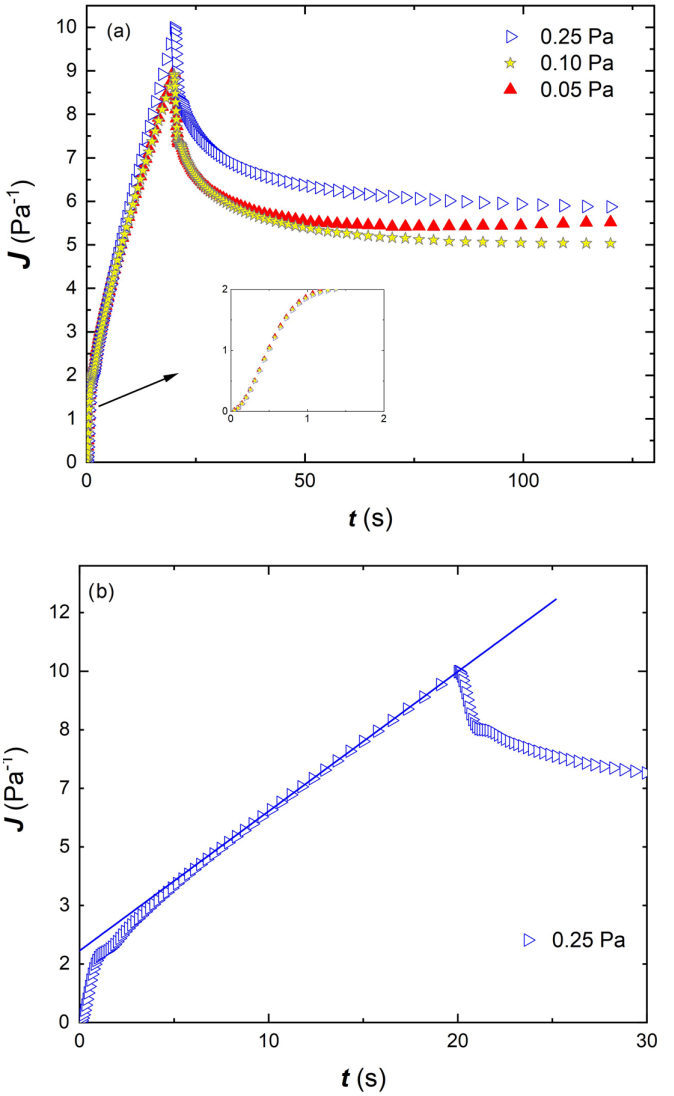

FIG. 3. Creep test results for 0.1 wt% XG in 1-1 GC. (a) Modulus of creep compliance and recovery as a function of time at different exposed shear stresses and (b) best linear fit of a tangential line to the creep modulus at 0.25 Pa.

After imposing constant shear stress, the material response can be measured in the form of creep compliance (J) and recovery, where

$$J(t,\ \tau_0) = \frac{\gamma_{12}(0,t)}{-\tau_0} = \frac{1}{\eta_0}(t+\lambda). \tag{10}$$

From (10) it is evident that by plotting J as a function of t, the relaxation time λ can be estimated using the slope $(1/\eta_0)$ and the intercept (λ/η_0). The relaxation time was estimated from the experimental data by drawing a tangential line on the creep compliance diagram and finding the slope and intercept of the best fit. Figure 3(a) shows the experimental results for creep and recovery compliances of 0.1 wt% XG in the 1-1 GC solution at three constant stresses. A tangential line is sketched on the creep compliance data in Fig. 3(b) for 0.25 Pa shear stress to determine λ and η_0. A

TABLE II. Parameters of creep experiment for different solutions. η_1: The highest measured viscosity from experiments. λ_{creep}: Creep relaxation time calculated from the intercept. $\eta_{0,\ creep}$: Zero shear viscosity calculated from the slope.

Material	τ_0 (Pa)	Slope $=\frac{1}{\eta_0}$	Intercept $=\frac{\lambda}{\eta_0}$	$\eta_{0,\ creep}$ (Pa s)	λ_{creep} (s)	η_1 (Pa s)	$\eta_{0,Carreau}$ (Pa s)
	0.03	0.4127	2.6275	2.42	6.37		
0.1 wt% XG in 1-1 GC	0.05	0.4123	2.4191	2.43	5.87	2.42	3.20
	0.10	0.4113	2.4600	2.43	5.98		
	0.03	0.7057	3.0618	1.42	4.34		
0.2 wt% XG	0.05	0.6388	3.1355	1.57	4.91	1.75	1.80
	0.10	0.6919	2.8028	1.45	4.05		
	0.50	0.6521	0.5579	1.53	0.86		
1.0 wt% PEO	0.25	0.6265	0.9311	1.60	1.49	1.17	1.50
	0.10	0.5755	1.2196	1.74	2.12		

similar procedure was followed at other constant shear stresses. The results for different solutions are summarized in Table II.

Since the magnitudes of λ and η_0 could slightly depend on the magnitude of the imposed shear stress, τ_0, η_0 was used as a control parameter and compared with the zero shear viscosity estimated from the best fit of the Carreau model. When a close agreement was achieved, we considered the relaxation time obtained from the creep experiment λ_{creep} to be acceptable. This was the case in the PEO solution. In the absence of a close agreement, we compared η_0 from creep experiments with the highest measured value of viscosity from steady shear results. This was the case in 0.1wt% XG in 1-1 GC solution, where η_0 from the creep test was 2.42 and 2.43 Pa s at $\tau_0 = 0.03$ and 0.05 Pa, respectively, while it was estimated to be 3.20 from Carreau curve-fitting parameters. The highest measured shear viscosity from steady shear results of Fig. 2 was 2.42 Pa s. Therefore, an average was taken between λ values from creep experiments which will result in $\lambda_{creep}= 6.07$ s. The error for the best fit of the tangential line to the experimental data was calculated using $R^2 = 1-\frac{\sum_{i=1}^{N}[f_{expt}(i)-f_{fit}(i)]^2}{(N-1)\sigma(f)}$, where N is the number of data points, f is the function value, which is the compliance modulus (J) in this case, the difference $f_{expt} - f_{fit}$ is called the residual, which is the difference between the experimental value f_{expt}, and f_{fit}, the fitted value of the function f, and $\sigma(f)$ is the variance of f. For all data reported in Table II, $R^2 \geqslant 0.998$.

We performed small-amplitude oscillatory shear measurements at room temperature to further investigate the validity of the obtained relaxation time from the creep experiments. Multimode generalized Maxwell constitutive Eqs. (11) and (12) were used to find the best fit of the experimental data, where, G' (Pa) and G'' (Pa) are the elastic and loss moduli, respectively, ω (rad/s) is the angular frequency, G_i (Pa) is the relaxation modulus, λ_i (s) is the relaxation time for mode i, and m is the number of modes. Using small-amplitude oscillatory shear (SAOS) data, the best fit of the multimodal generalized Maxwell model can provide different values for λ. Since the frequency sweep data were obtained over three decades of frequency, we used three modes of the generalized Maxwell model for comparison. The least-squares function in *Matlab* (MathWorks) was used for curve-fitting purposes, and the parameters for the best fit are reported in Table III. The longest relaxation time from curve fitting was taken for comparison with λ_{creep} in Table II:

$$G' = \sum_{i=1}^{m} \frac{G_i\, {\lambda_i}^2 \omega^2}{1 + \omega^2 \lambda_i^2}, \tag{11}$$

$$G'' = \sum_{i=1}^{m} \frac{G_i\, \lambda_i\, \omega}{1 + \omega^2 \lambda_i^2}. \tag{12}$$

TABLE III. Fitting parameters for three-mode generalized Maxwell model and the relaxation time from the creep tests.

Material	G_1 (Pa)	G_2 (Pa)	G_3 (Pa)	λ_1 (s)	λ_2 (s)	λ_3 (s)	λ_{creep} (s)
1.0 wt% PEO	0.79	2.19	6.44	1.51	0.21	0.04	0.86
0.1 wt% XG in 1-1 GC	0.43	0.77	2.47	3.04	0.28	0.03	6.07
0.2 wt% XG	No data is available						4.91

The experimental SAOS results, along with the predictions of the three-mode Maxwell model, are illustrated in Fig. 4(a) for 0.1 wt% XG in 1-1 GC and in Fig. 4(b) for 1.0 wt% PEO solution, and the fitting parameters are summarized in Table III. We observed a difference between the relaxation time from the creep experiments and the three-mode Maxwell model from the results reported in this table. In the case of the PEO solution, λ was 0.86 s from creep experiments and 1.51 s for the longest Maxwell relaxation time. In the case of 0.1 wt% XG in 1-1 GC, $\lambda_{creep} = 6.07$ s while the longest relaxation time from the Maxwell model was $\lambda = 3.04$ s . These values compare well with literature. For 3390 ppm (or 0.34 wt%) PEO with 2×10^6 g/mol molecular weight in a solvent containing 60 wt% de-ionized (DI) water and 40 wt% PEG (with $M_w = 8000$ g/mol), the longest Maxwell relaxation time was 0.328 and 0.287 s using SAOS measurements in Refs. [59,60], respectively.

For the PEO solution and 0.1 wt% XG in 1-1 GC, the relaxation time was taken as an average of the longest relaxation time of the Maxwell model and the creep tests. For the 0.2 wt% XG solution, we considered the relaxation time from the creep test to be acceptable since the SAOS results for this solution are missing. Therefore λ was set to 1.185 s for PEO, 4.56 s for 0.1 wt% XG in 1-1 GC, and 4.91 s for 0.2 wt% XG.

B. Flow visualization

Following rheological characterization, we ran the polymer solutions through the microchannels. Flow visualization experiments were performed, and videos were captured in the central plane of the channels (at $z = 0$). Capturing videos at the half depth of the channels resulted in some optical distortion near the edges of some channels and low resolution of the streak images in some snapshots. The flow rate was increased at 10 μl/h increments up to 100 μl/h, then at 100 μl/h increments up to the flow rate of 1000 μl/h, and at 1000 μl/h increments for higher ranges of flow rates. The snapshots of some recorded videos are demonstrated in Fig. 5–7 at various flow rates. In all cases, the flow was from left to right. It was observed that vortices formed upstream of the obstacle at a different onset flow rate in each solution. The vortex length increased with increasing flow rate. When the vortex length was much longer than the field of view, it was not easy to measure the vortex length accurately; therefore, only the range of flow rates where the vortex length could be reliably measured is considered and reported for each solution.

The results for 0.2 wt% XG solutions are shown in Fig. 5, where the flow rate changes from 300 μl/h ($\mathrm{Re} = 0.013$, $\mathrm{Wi_{eff}} = 362$) to 2740 μl/h ($\mathrm{Re} = 0.4756$, $\mathrm{Wi_{eff}} = 3304$). The vortex was first observed at 200 μl/h ($\mathrm{Re} = 0.0068$). The size of the vortex gradually increased with increasing the flow rate. Some individual fluorescent particles can be detected in the vortex from the snapshots due to the much slower fluid flow than the main flow stream, where only streak lines can be observed as the fluid approaches the constriction. Through the entire range of flow rates shown in this figure, the flow remained stable and the vortex size stayed unchanged over time, at each flow rate.

Similarly, in 0.1 wt% XG in 1-1 GC, the initial corner vortex was observed upstream of the obstacle at flow rates as low as 200 μl/h ($\mathrm{Re} \sim 0.0046$, $\mathrm{Wi_{eff}} = 224$). Figure 6 displays streak images of flow in the channels for 0.1 wt% XG in 1-1 GC at various flow rates spanning between 400 μl/h ($\mathrm{Re} = 0.0145$, $\mathrm{Wi_{eff}} = 487$) and 2000 μl/h ($\mathrm{Re} = 0.16$, $\mathrm{Wi_{eff}} = 2237$). The size of the corner vortex grew with increasing flow rate. However, compared to the results reported in Fig. 5, the vortex length was much longer at similar flow rates, even though 0.1 wt% XG in 1-1 GC is slightly

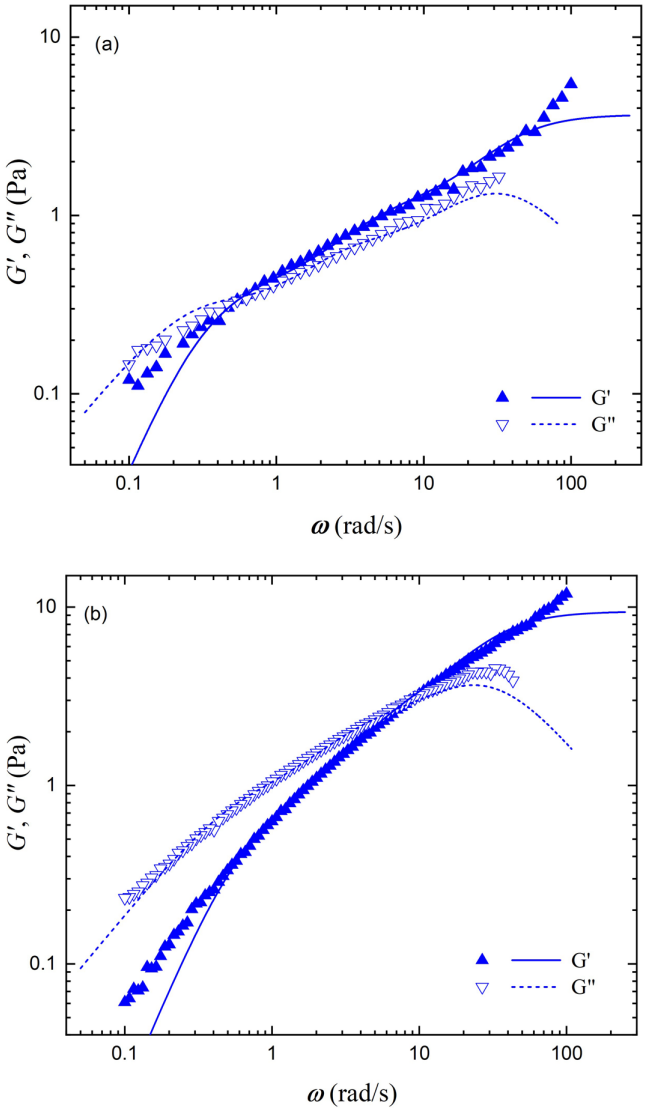

FIG. 4. Small-amplitude oscillatory shear results for (a) 0.1 wt% XG in 1-1 GC and (b) 1.0 wt% PEO. The data points represent experimental results, and the lines show the best fit with a three-mode generalized Maxwell model.

less shear thinning ($n = 0.4$) compared to the 0.2 wt% XG solution ($n = 0.34$). This observation could be due to the higher elasticity of the 0.1 wt% XG solution due to the addition of glycerol.

Figure 7 represents the streak images of flow in the channels for 1.0 wt% PEO at flow rates spanning from 500 μl/h (Re = 0.0067, $\mathrm{Wi_{eff}} = 134$) to 15 000 μl/h (Re = 1.06, $\mathrm{Wi_{eff}} = 4020$). In this solution, the initial corner vortices were observed at flow rates slightly higher than 500 μl/h (Re $\sim$ 0.0067) upstream of the obstacle. Interestingly, the size of the corner vortex in the PEO solution was much smaller than in the xanthan gum solutions at similar flow rates; we also noticed that the vortex size remained relatively constant for the range of flow rates between 1500 and 5000 μl/h. At relatively higher flow rates (greater than 5000 μl/h), the vortex size began to grow, as is shown in Figs. 7(e) and 7(f). At high enough flow rates (greater than 15 000 μl/h or Re $\geqslant$ 1.06),

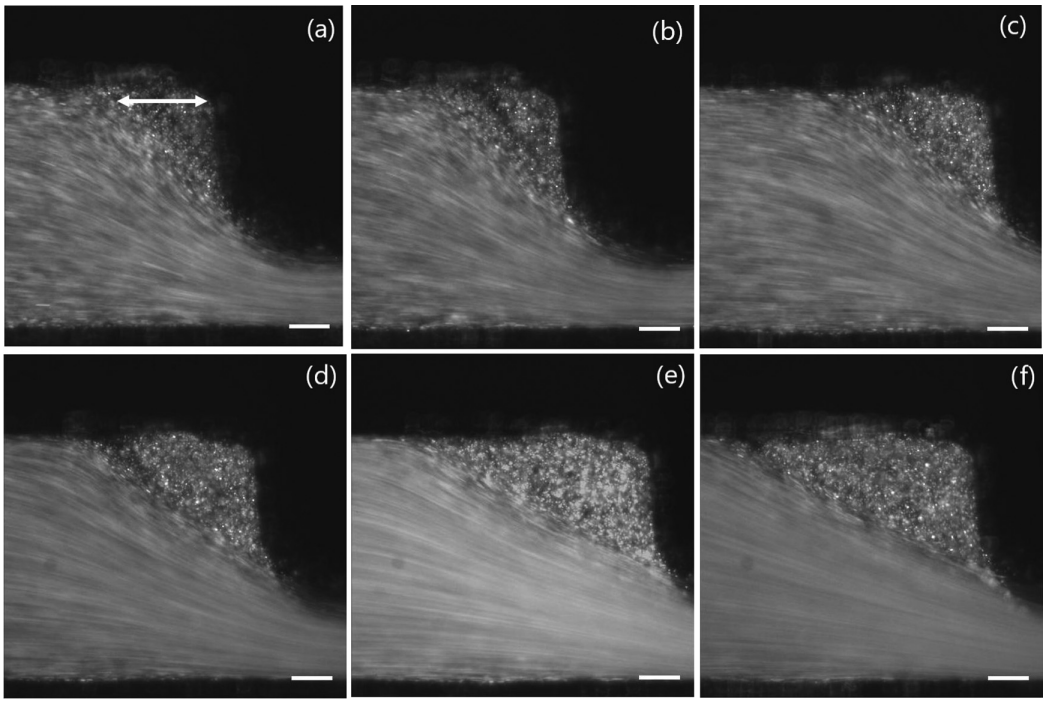

FIG. 5. Streak images of flow in channels for 0.2 wt% XG at different flow rates. (a) $Q = 300$ μl/h, Re $= 0.013$, $\mathrm{Wi_{eff}} = 362$; (b) $Q = 400$ μl/h, Re $= 0.021$, $\mathrm{Wi_{eff}} = 482$; (c) $Q = 500$ μl/h, Re $= 0.030$, $\mathrm{Wi_{eff}} = 603$; (d) $Q = 1000$ μl/h, Re $= 0.094$, $\mathrm{Wi_{eff}} = 1206$; (e) $Q = 2000$ μl/h, Re $= 0.287$, $\mathrm{Wi_{eff}} = 2412$; and (f) $Q = 2740$ μl/h, Re $= 0.476$, $\mathrm{Wi_{eff}} = 3304$. The scale bars show 100 μm. The double-sided arrow in (a) shows the vortex length (L_v). The contraction ratio is 4.675.

the flow of PEO solutions became time dependent, and the size of the corner vortex increased more dramatically while fluctuating. Figures 7(g) and 7(h) exhibit the flow near the constriction at 25 000 μl/h (Re $= 2.25$, Wi $= 6701$) and 35 000 μl/h (Re $= 3.7$, Wi $= 9381$), respectively. The time-dependent flow was also three dimensional as manifested by some particles migrating from the lower wall to the upstream vortex. The yellow streaklines in Figs. 7(i) and 7(j) show evidence for particle migration from the lower wall towards the corner upstream vortex due to this three dimensional motion. From flow visualization experiments reported in Figs. 5–7 performed over a wide range of Re ($0.0046 \lesssim \mathrm{Re} \lesssim 3.7$) and $\mathrm{Wi_{eff}}$ ($134 \leqslant \mathrm{Wi_{eff}} \lesssim 9381$), no lip vortex was observed for any of the solutions, which is consistent with numerical predictions of Alves *et al.* [32] for a PTT fluid in a geometry with CR ~ 4 and a solvent viscosity ratio of $\beta = 1/9$. In the present experiments, the solvent viscosity ratio was much smaller, ranging from 0.0006 to 0.002. The shape of the vortex in the xanthan gum solutions is triangular, while the vortex looks concave in the PEO solution.

To further analyze the observations from the flow visualization experiments and make comparisons at similar flow conditions, the dimensionless vortex length $\chi = L_v/W_u$ is plotted as a function of dimensionless numbers Re and $\mathrm{Wi_{eff}}$ in Figs. 8(a) and 8(b), respectively.

The data points represent the experimentally measured results, and the lines represent the best logarithmic fit for xanthan solutions and a second-degree polynomial fit for the PEO solution. From Fig. 8(a), both xanthan gum solutions exhibit a significant vortex growth over a narrow range of Re (up to Re ~ 0.5) compared to the PEO solution; however, this observation is more pronounced in the case of 0.1 wt% XG solution. The 0.1 wt% XG solution exhibits a more dramatic growth in vortex size over a narrow range of Wi, distinguishing its behavior from the other two solutions. By extrapolating the best fit of experimental data, one can conclude that the vortex length in 0.1 wt%

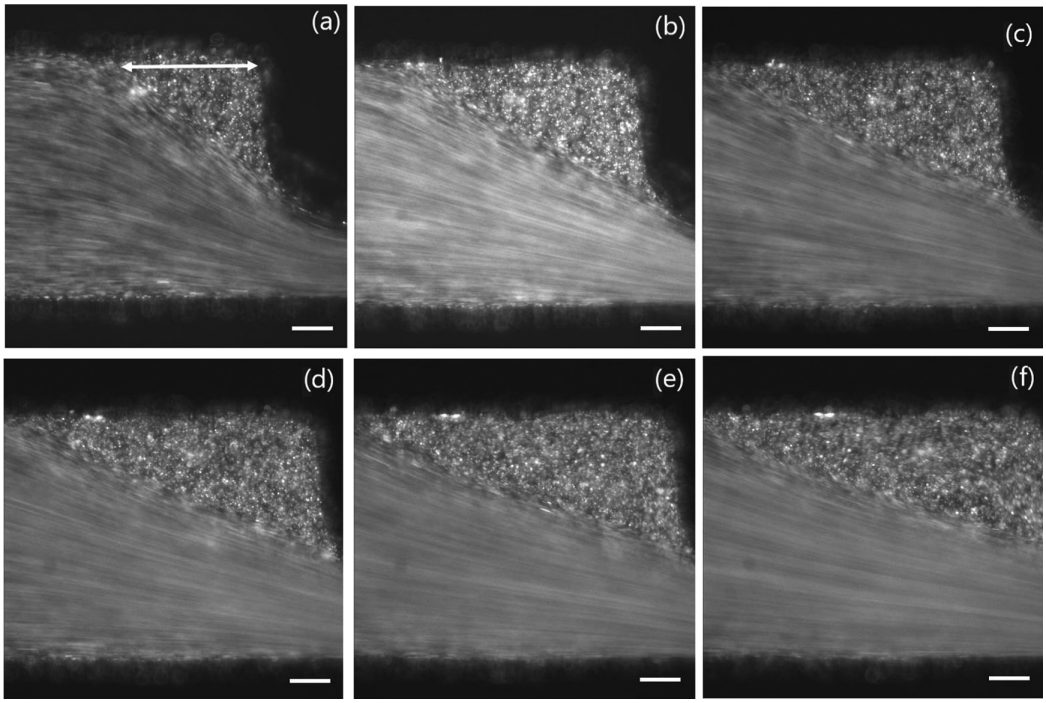

FIG. 6. Streak images of flow in the channels for 0.1 wt% XG in 1-1 GC at different flow rates. (a) $Q = 400$ μl/h, Re $= 0.0145$, $\mathrm{Wi_{eff}} = 447$; (b) $Q = 700$ μl/h, Re $= 0.034$, $\mathrm{Wi_{eff}} = 783$; (c) $Q = 850$ μl/h, Re $= 0.0456$, $\mathrm{Wi_{eff}} = 951$; (d) $Q = 1000$ μl/h, Re $= 0.058$, $\mathrm{Wi_{eff}} = 1119$; (e) $Q = 1500$ μl/h, Re $= 0.106$, $\mathrm{Wi_{eff}} = 1678$; (f) $Q = 2000$ μl/h, Re $= 0.16$, $\mathrm{Wi_{eff}} = 2237$. The scale bars show 100 μm. The double-sided arrow in (a) shows the vortex length (L_v). The contraction ratio is 4.675.

XG will only reach a plateau at a much higher range of Re and Wi. In other words, the vortex growth mechanism in this solution will extend over an extensive range of Re and $\mathrm{Wi_{eff}}$. The vortex size increases more gradually in 0.2 wt% XG solution when $\mathrm{Wi_{eff}}$ spans between 360 to 3300 and seems to reach a plateau at higher Weissenberg numbers. The PEO solution demonstrates a very different behavior; for Re $\leqslant 0.2$ and $\mathrm{Wi_{eff}} \leqslant 1500$, the vortex size is relatively independent of Re and $\mathrm{Wi_{eff}}$ as is shown in Figs. 8(a) and 8(b) and a pronounced vortex growth does not occur until Re > 0.4 and $\mathrm{Wi_{eff}} > 2000$. At much higher Re (Re > 1) and $\mathrm{Wi_{eff}}$ ($\mathrm{Wi_{eff}} > 4000$), a time-dependent flow behavior as manifested by vortex size fluctuations was observed in the microchannels.

Based on the results reported in Fig. 8, there is a clear difference in flow behavior of the xanthan gum and the PEO solutions. We believe this difference originates from the difference in their molecular structure and flexibility. The estimated extensibility parameter for PEO was 5000 and much higher than 33.5 for xanthan gum. Therefore, the PEO molecules are expected to be more flexible and more resistant to orientation in the flow direction compared to much shorter and less flexible xanthan gum molecules. In addition, increasing the solvent viscosity in 0.1 wt% XG in 1-1 GC should present more resistance to orientation in the flow direction. More careful experimental investigation (e.g., by light scattering techniques) and theoretical modeling (e.g., by incorporating molecular dynamics simulations) are necessary to further explore the involved mechanisms which is beyond the scope of this work. The instabilities observed in PEO solutions may not solely be due to the increase in flow rate; they may have to do with the events downstream of the constriction. Such events include relaxation of polymer molecules in the constriction, changes in polymer chain orientation in the constriction due to very high shear rates and secondary stretch, and changes in orientation of the polymer chains in the expansion region as suggested by Rodd *et al.* [43] and

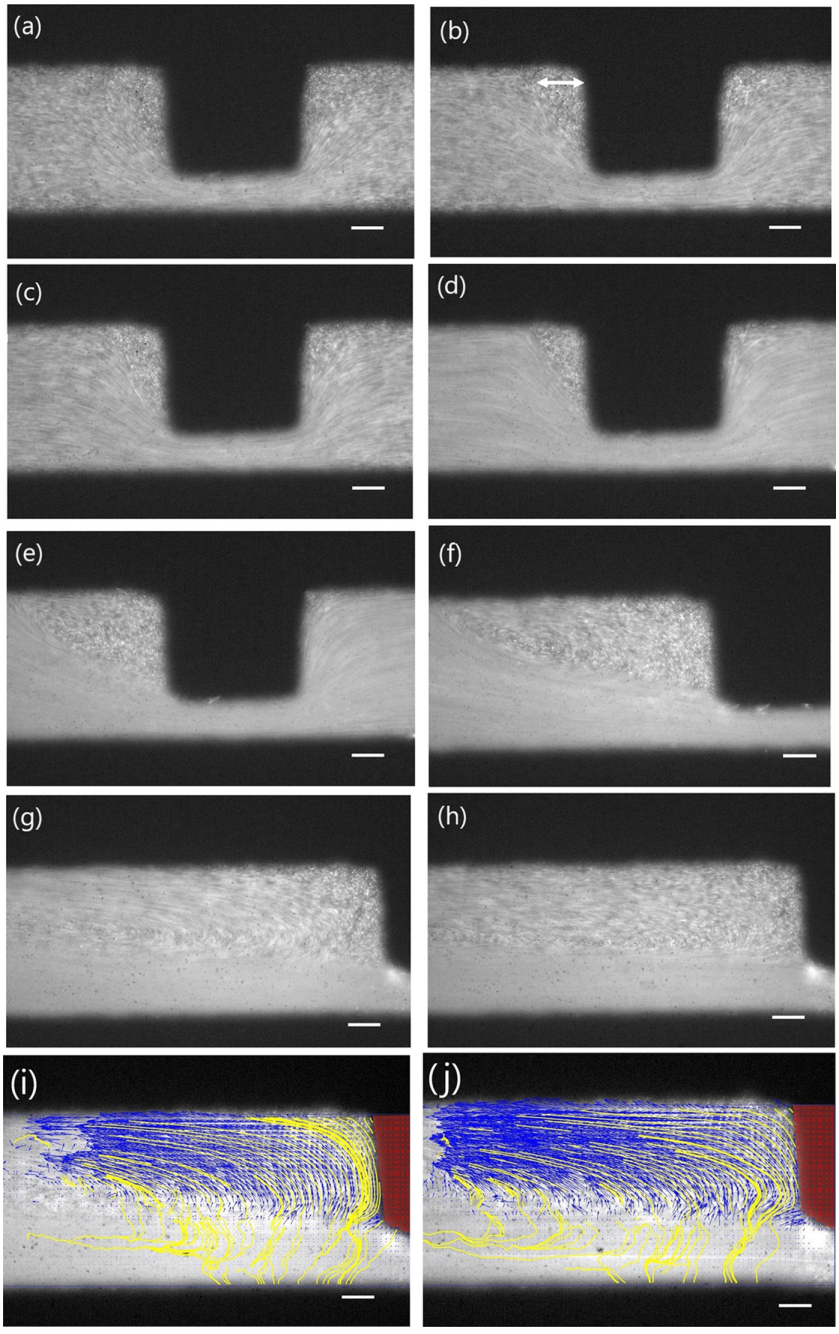

FIG. 7. Streak images (a)–(h) of flow in the channel for 1.0 wt% PEO at different flow rates and streaklines (i, (j) at high flow rates. (a) $Q = 500\ \mu$l/h, Re $= 0.0067$, $\mathrm{Wi_{eff}} = 134$; (b) $Q = 1000\ \mu$l/h, Re $= 0.0188$, $\mathrm{Wi_{eff}} = 268$; (c) $Q = 2000\ \mu$l/h, Re $= 0.053$, $\mathrm{Wi_{eff}} = 536.4$; (d) $Q = 5000\ \mu$l/h, Re $= 0.2076$, $\mathrm{Wi_{eff}} = 1341$; (e) $Q = 10\,000\ \mu$l/h, Re $= 0.5812$, $\mathrm{Wi_{eff}} = 2680$; (f) $Q = 15\,000\ \mu$l/h, Re $= 1.06$, $\mathrm{Wi_{eff}} = 4020$; (g) and (i) $Q = 25\,000\ \mu$l/h, Re $= 2.25$, $\mathrm{Wi_{eff}} = 6701$; (h) and (j) $Q = 35\,000\ \mu$l/h, Re $= 3.7$, $\mathrm{Wi_{eff}} = 9387$. The scale bars show 100 μm. The double-sided arrows show the vortex length (L_v). The contraction ratio of channels is 4.31.

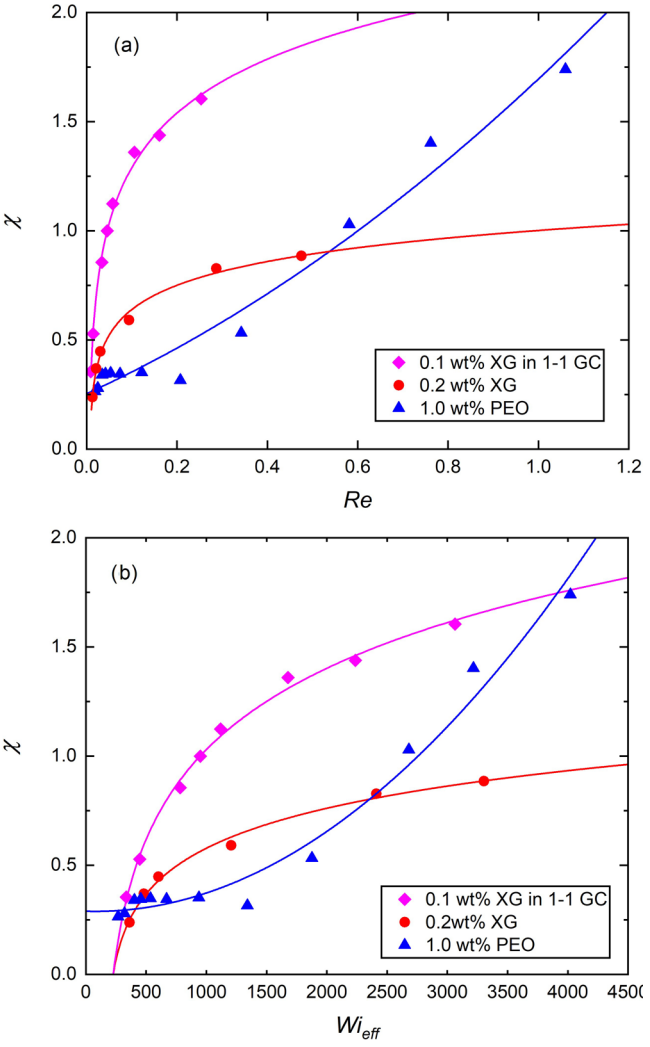

FIG. 8. Dimensionless vortex length as a function of (a) Re and (b) Wi_{eff} for 1.0 wt% PEO, 0.2 wt% XG, and 0.1 wt% XG in 1-1 GC. The lines show a logarithmic trend in the experimental results for the xanthan gum solutions and a second-degree polynominal for the PEO solution.

Rothstein and McKinley [39]. PEO may also have experienced chain scission due to high shear rates in the constriction, which further affects flow patterns upstream of the constriction. A recent study by Raihan *et al.* [44] on the effect of constriction length on both contraction and expansion flows of several fluids exhibited that unlike the xanthan gum, the PEO solution showed constriction length dependent instabilities for the contraction flow.

Moreover, we did not observe any lip vortex or divergent flow, signature features for inertioelastic flow behaviors in the entry flow of viscoelastic fluids. It is possible that due to the absence of inertia at Re < 1.0, lip vortices and diverging flow were not present in our geometry; however, more experiments need to be performed over a wider range of fluid concentrations, flow rates, and contraction ratios before we rule out the possibility of having them in this geometry.

From the results reported in Fig. 8, one can conclude that elasticity is central in the formation and growth of vortices. Our results are comparable to Sousa *et al.* [23], who investigated a Newtonian and shear-thinning fluid flow in a square-square microfluidic abrupt contraction/expansion flow over several contraction ratios (i.e., CR $\sim$ 2.4, 4, 8, and 12). For the shear-thinning fluid, a corner vortex was observed independent of the contraction ratio. They observed that by increasing the elasticity of the flow, the vortex size strongly increased while still at low Re, until an elastic instability emerged and the flow became time-dependent at De $\approx$ 200, 300, 70, and 450 for CR = 2.4, 4, 8, and 12, respectively. In our reported results, the instabilities emerged at Re $>$ 1 and $\mathrm{Wi_{eff}} > 4000$ in the PEO solution. Similarly, Haward *et al.* [21] investigated flow instabilities of polystyrene (PS) solutions in a similar range of Re ($0.07 < \mathrm{Re} < 11.2$) and Wi ($8.7 < \mathrm{Wi} < 1562$) but over a narrow range of elasticity numbers ($31 < \mathrm{El} < 295$) compared to our case. They reported flow transitions spanning between Newtonian-like flow (no corner vortex upstream of the constriction) to unstable flow at the critical Wi = 150 and unstable flow to vortex growth in the upstream salient corners at the critical Wi = 400. They showed that transitions between the flow regimes scaled with Wi, independent of El, revealing the importance of elastic forces compared to inertial effects in all the fluids they studied. In addition, by combining birefringence analysis with flow measurements, they estimated the macromolecular strain values in the microchannel constriction. For the Newtonian-like flow regime ($\mathrm{Wi} \leqslant 150$), this strain value was zero but increased with the emergence of the unstable flow and reached a plateau value at the onset of vortex growth ($\mathrm{Wi} \geqslant 400$).

We believe any potential imperfections in the walls of the constriction could not be a reason for major differences in the flow behavior of the solutions. This argument is supported by observations of Evans and Walters [3], who reported that in CR $\sim$ 16 : 1, small changes in the corner geometry, such as ramped lips and/or uneven reentrant corners or nonvertical walls, can influence the global flow behavior in Boger fluids but have little effect in shear-thinning fluids.

Moreover, no divergent flow or vortex truncation due to increasing flow rate (or Re) was observed. In benchmark planar contraction/expansion geometries with 4:1 contraction ratios, Goertler-like or lip vortices [37,38] are typically observed in shear-thinning fluids for aspect ratios (h/w_c) higher than 20. In our geometry, no Goertler-like or lip vortices were observed and the aspect ratio was slightly greater than 2.0.

Finally, Figs. 9(a) and 9(b) represent the results for $\mathrm{Wi_{eff}}$ versus Re and El number versus $\mathrm{Wi_{eff}}$, respectively, where a vortex with measurable length was observed in each solution. Figure 9(a) demonstrates the onset of vortex formation and growth is achieved at lower Re and $\mathrm{Wi_{eff}}$ for 0.1 wt% XG in 1-1 GC compared to the other two solutions and 0.2 wt% XG compared to the PEO solution. For each solution, we estimated El at Re = 0.03 to be 23 054 for 0.1 wt% XG in 1-1 GC, 19 920 for 0.2 wt% XG, and 11 667 for 1.0 wt% PEO solutions. This reveals that the onset of vortex formation transitions to lower Re and $\mathrm{Wi_{eff}}$ as the elasticity of the solutions increase. The trend line in Fig. 9(b) represents the best fit with $\mathrm{El} = a\ \mathrm{Wi_{eff}^{-b}}$, where $a = 9.34 \times 10^{10}$ and $b = 2.06$ for 1.0 wt% PEO solution, $a = 5.58 \times 10^{9}$ and $b = 1.62$ for 0.2 wt% XG solution, and $a = 1.44 \times 10^{12}$ and $b = 2.12$ for 0.1 wt% XG in 1-1 GC solution. In all three cases, there exists a strong dependence of El on $\mathrm{Wi_{eff}}$. From this figure, in the creeping flow region ($\mathrm{Re} \ll 1.0$ or low $\mathrm{Wi_{eff}}$), the elasticity of 0.1 wt% XG in 1-1 GC is about 10 000 more than 0.2 wt% XG and about 25 000 more than the PEO solution. As the viscous forces become less important (higher $\mathrm{Wi_{eff}}$), the elasticity numbers decay gradually to a constant value and become more similar as $\mathrm{Wi_{eff}} \to \infty$.

We also emphasize that we did not observe any downstream vortices in the range of Re and Wi studied. Our observations are consistent with Rodd *et al.* [17], who studied the flow behavior of weakly elastic PEO solutions in 16:1:16 planar contraction/expansion geometries. They showed that elasticity is key to generating strong viscoelastic effects, and a similar behavior may not be observed at the macroscale. For non-Newtonian fluids, they showed that downstream vortices did not form for Re $<$ 50. In our experiments, the highest achievable Re was about 3.7. The results reported in Fig. 9 further confirm our interpretations regarding the importance of elasticity in vortex formation and growth.

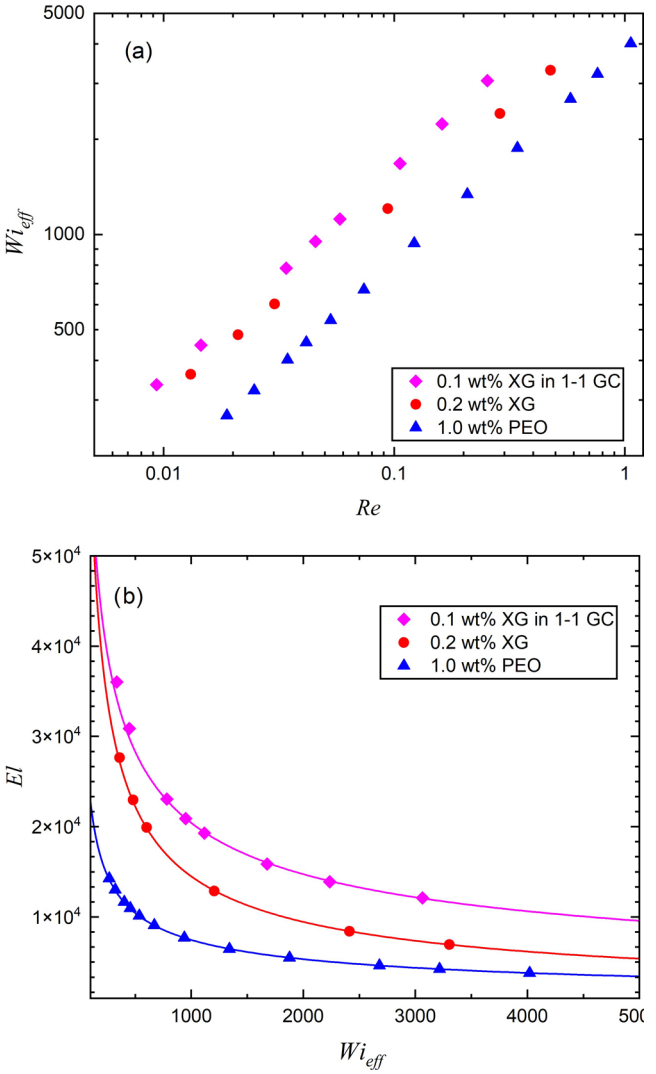

FIG. 9. (a) $\mathrm{Wi_{eff}}$ vs Re and (b) El vs $\mathrm{Wi_{eff}}$ for 1.0 wt% PEO, 0.2 wt% XG, and 0.1 wt% XG in 1-1 GC. The data points represent experimental results where a vortex with measurable length was observed. The trend lines show the best power-law fit with the experimental data ($\mathrm{El} = a\ \mathrm{Wi_{eff}^{-b}}$).

IV. CONCLUDING REMARKS

Despite extensive work in the entry flow of non-Newtonian fluids in abrupt contraction/expansion geometries, unexplored features and unexplained mechanisms make these flow interesting to further investigate in various fluids, geometries, and flow kinematics. Besides the type of the fluid, contraction ratio [45], and aspect ratio [7], different ways of characterizing some fluid properties such as the relaxation time can result in different interpretations of the flow behavior. In addition, the competition between shear and extension near the flow reentrance presents additional complications to the flow behavior that cannot be easily explored in a rheometer. These flow features call for further investigation to make generalizable conclusions independent of the fluid type or geometry and map different flow regimes in Wi-Re space more accurately.

Experiments were performed to compare the flow behavior of several shear-thinning fluids of xanthan gum and polyethylene oxide with relatively similar shear thinning index spanning from 0.34 to 0.50 in a microfluidic planar contraction/expansion geometry with a nominal contraction ratio of 4. The geometry differs from those examined previously in the literature. In particular, in previous studies, the flow has been symmetric about the flow centerline, while in the present work that line is replaced by a solid boundary. We explored a wide range of Re ($0.0046 \lesssim \mathrm{Re} \lesssim 3.7$) and $\mathrm{Wi}_{\mathrm{eff}}$ ($134 \leqslant \mathrm{Wi}_{\mathrm{eff}} \lesssim 9381$) for shear-thinning fluids. From flow visualization experiments, we observed that for the weakly elastic aqueous solutions, vortices form upstream of the constriction and the vortex length grew by increasing the Re, and $\mathrm{Wi}_{\mathrm{eff}}$. The onset of vortex formation and growth shifted to lower Re and Wi by increasing the elasticity and the elasticity number El. This observation is consistent with Rodd *et al.* [17] and can be attributed to the importance of the fluid properties and the characteristic length of the device in vortex formation independent of flow kinematics, or simply El. We believe the higher extensibility and therefore flexibility of PEO molecules introduces more resistance to molecular orientation in the flow direction, which may have been the reason to postpone vortex formation and growth to higher Re and $\mathrm{Wi}_{\mathrm{eff}}$ compared to xanthan gum solutions. It is noteworthy that the two xanthan gum solutions have similar shear rheology but different El, and the flow visualization experiments revealed a significant difference between their flow behaviors around the obstacle in the microchannels. The difference in the vortex size in xanthan gum solutions shows the importance of solvent viscosity in vortex formation and the higher inherent elasticity of the solution. In addition, increasing the solvent viscosity in 0.1 wt% XG in 1-1 GC should present more resistance to orientation in the flow direction.

Moreover, no divergent flow or vortex truncation due to increasing flow rate (or Re) was observed, which might be due to very low Re used in this study and the creeping nature of flow. In addition, no Goertler-like or lip vortices were observed in our geometry with the aspect ratio slightly greater than 2.0. It is noteworthy that Goertler-like or lip vortices were observed in shear-thinning fluids in benchmark contraction/expansion geometries with 4:1 contraction ratios when the aspect ratios (h/w_c) exceeded 20 [37–39]. We also observed a time-dependent flow in PEO solutions at relatively high Re and Wi numbers from flow visualization experiments. The mechanism of time-dependent chaotic flow is not very clear and needs further investigation. Perhaps careful pressure measurements in different regions of the geometry combined with flow visualization and particle image velocimetry can shed more light on these observations and more vigorously support future simulations. Chaotic flow instabilities can offer advantages in different applications such as micromixing, heat, and mass transfer by employing elastic non-Newtonian fluids [25]. However, to make the characterization of extensional properties more accurate, it is essential to avoid instabilities in microrheometry; other industrial applications, including inkjet printing, roll coating, and fiber spinning, call for minimizing flow instabilities to the extent possible to make optimal products. Understanding the onset and mechanisms of flow instabilities can shed light on designing more efficient industrial processes and optimal products and can pave the way to design microrheometric devices for weakly elastic dilute polymer solutions.

ACKNOWLEDGMENT

The authors acknowledge the financial support from Fonds Québécois de la Recherche sur la Nature et les Technologies (FQRNT) and Procter and Gamble.

[1] P. H. S. Picciani, E. S. Medeiros, Z. Pan, D. F. Wood, W. J. Orts, L. H. C. Mattoso, and B. G. Soares, Structural, electrical, mechanical, and thermal properties of electrospun poly(lactic acid)/polyaniline blend fibers, Macromol. Mater. Eng. **295**, 618 (2010).

[2] H. Nguyen and D. V. Boger, The kinematics and stability of die entry flows, J. Non-Newtonian Fluid Mech. **5**, 353 (1979).

[3] R. E. Evans and K. Walters, Flow characteristics associated with abrupt changes in geometry in the case of highly elastic liquids, J. Non-Newtonian Fluid Mech. **20**, 11 (1986).
[4] R. E. Evans and K. Walters, Further remarks on the lip-vortex mechanism of vortex enhancement in planar-contraction flows, J. Non-Newtonian Fluid Mech. **32**, 95 (1989).
[5] S. Nigen and K. Walters, Viscoelastic contraction flows: Comparison of axisymmetric and planar configurations, J. Non-Newtonian Fluid Mech. **102**, 343 (2002).
[6] M. S. N. Oliveira, M. A. Alves, F. T. Pinho, and G. H. McKinley, Viscous flow through microfabricated hyperbolic contractions, Exp. Fluids **43**, 437 (2007).
[7] M. S. N. Oliveira, L. E. Rodd, G. H. McKinley, and M. A. Alves, Simulations of extensional flow in microrheometric devices, Microfluid. Nanofluid. **5**, 809 (2008).
[8] S. J. Haward, M. S. N. Oliveira, M. A. Alves, and G. H. McKinley, Optimized Cross-Slot Flow Geometry for Microfluidic Extensional Rheometry, Phys. Rev. Lett. **109**, 128301 (2012).
[9] F. J. Galindo-Rosales, M. A. Alves, and M. S. N. Oliveira, Microdevices for extensional rheometry of low viscosity elastic liquids: A review, Microfluid. Nanofluid. **14**, 1 (2013).
[10] K. Zografos, S. J. Haward, and M. S. N. Oliveira, Optimised multi-stream microfluidic designs for controlled extensional deformation, Microfluid. Nanofluid. **23**, 131 (2019).
[11] S. C. Hur, A. J. Mach, and D. Di Carlo, High-throughput size-based rare cell enrichment using microscale vortices, Biomicrofluidics **5**, 022206 (2011).
[12] A. Haller, A. Spittler, L. Brandhoff, H. Zirath, D. Puchberger-Enengl, F. Keplinger, and M. J. Vellekoop, Microfluidic vortex enhancement for on-chip sample preparation, Micromachines **6**, 239 (2015).
[13] A. T. S. Cerdeira, J. B. L. M. Campos, J. M. Miranda, and J. D. P. Araújo, Review on microbubbles and microdroplets flowing through microfluidic geometrical elements, Micromachines **11**, 201 (2020).
[14] C. A. Browne, A. Shih, and S. S. Datta, Pore-scale flow characterization of polymer solutions in microfluidic porous media, Small **16**, 1903944 (2020).
[15] C. A. Browne, A. Shih, and S. S. Datta, Bistability in the unstable flow of polymer solutions through pore constriction arrays, J. Fluid Mech. **890**, A2 (2020).
[16] P. P. Jagdale, D. Li, X. Shao, J. B. Bostwick, and X. Xuan, Fluid rheological effects on the flow of polymer solutions in a contraction–expansion microchannel, Micromachines **11**, 278 (2020).
[17] L. E. Rodd, T. P. Scott, D. V. Boger, J. J. Cooper-White, and G. H. McKinley, The inertio-elastic planar entry flow of low-viscosity elastic fluids in micro-fabricated geometries, J. Non-Newtonian Fluid Mech. **129**, 1 (2005).
[18] L. E. Rodd, J. J. Cooper-White, D. V. Boger, and G. H. McKinley, Role of the elasticity number in the entry flow of dilute polymer solutions in micro-fabricated contraction geometries, J. Non-Newtonian Fluid Mech. **143**, 170 (2007).
[19] S. Gulati, S. J. Muller, and D. Liepmann, Direct measurements of viscoelastic flows of DNA in a 2:1 abrupt planar micro-contraction, J. Non-Newtonian Fluid Mech. **155**, 51 (2008).
[20] P. C. Sousa, P. M. Coelho, M. S. N. Oliveira, and M. A. Alves, Three-dimensional flow of Newtonian and Boger fluids in square–square contractions, J. Non-Newtonian Fluid Mech. **160**, 122 (2009).
[21] S. J. Haward, Z. Li, D. Lighter, B. Thomas, J. A. Odell, and X.-F. Yuan, Flow of dilute to semi-dilute polystyrene solutions through a benchmark 8:1 planar abrupt micro-contraction, J. Non-Newtonian Fluid Mech. **165**, 1654 (2010).
[22] O. L. Hemminger, P. E. Boukany, S.-Q. Wang, and L. J. Lee, Flow pattern and molecular visualization of DNA solutions through a 4:1 planar micro-contraction, J. Non-Newtonian Fluid Mech. **165**, 1613 (2010).
[23] P. C. Sousa, P. M. Coelho, M. S. N. Oliveira, and M. A. Alves, Effect of the contraction ratio upon viscoelastic fluid flow in three-dimensional square–square contractions, Chem. Eng. Sci. **66**, 998 (2011).
[24] A. Lanzaro and X.-F. Yuan, Effects of contraction ratio on non-linear dynamics of semi-dilute, highly polydisperse PAAm solutions in microfluidics, J. Non-Newtonian Fluid Mech. **166**, 1064 (2011).
[25] F. J. Galindo-Rosales *et al.*, Viscoelastic instabilities in micro-scale flows, Exp. Therm. Fluid Sci. **59**, 128 (2014).
[26] R. M. Matos, M. A. Alves, and F. T. Pinho, Instabilities in micro-contraction flows of semi-dilute CTAB and CPyCl solutions: Rheology and flow instabilities, Exp. Fluids **60**, 145 (2019).

[27] S. Wu *et al.*, Polymer effects on viscoelastic fluid flows in a planar constriction microchannel, J. Non-Newtonian Fluid Mech. **290**, 104508 (2021).
[28] D. W. Carlson, A. Q. Shen, and S. J. Haward, Microtomographic particle image velocimetry measurements of viscoelastic instabilities in a three-dimensional microcontraction, J. Fluid Mech. **923**, R6 (2021).
[29] L. Casanellas, M. A. Alves, R. J. Poole, S. Lerouge, and A. Lindner, The stabilizing effect of shear thinning on the onset of purely elastic instabilities in serpentine microflows, Soft Matter **12**, 6167 (2016).
[30] M. A. Alves, F. T. Pinho, and P. J. Oliveira, Effect of a high-resolution differencing scheme on finite-volume predictions of viscoelastic flows, J. Non-Newtonian Fluid Mech. **93**, 287 (2000).
[31] M. A. Alves, P. J. Oliveira, and F. T. Pinho, Benchmark solutions for the flow of Oldroyd-B and PTT fluids in planar contractions, J. Non-Newtonian Fluid Mech. **110**, 45 (2003).
[32] M. A. Alves, P. J. Oliveira, and F. T. Pinho, On the effect of contraction ratio in viscoelastic flow through abrupt contractions, J. Non-Newtonian Fluid Mech. **122**, 117 (2004).
[33] M. A. Alves and R. J. Poole, Divergent flow in contractions, J. Non-Newtonian Fluid Mech. **144**, 140 (2007).
[34] G. H. McKinley, W. P. Raiford, R. A. Brown, and R. C. Armstrong, Nonlinear dynamics of viscoelastic flow in axisymmetric abrupt contractions, J. Fluid Mech. **223**, 411 (1991).
[35] P. J. Oliveira and F. T. Pinho, Plane contraction flows of upper convected Maxwell and Phan-Thien–Tanner fluids as predicted by a finite-volume method, J. Non-Newtonian Fluid Mech. **88**, 63 (1999).
[36] P. J. Cable and D. V. Boger, A comprehensive experimental investigation of tubular entry flow of viscoelastic fluids: Part I. Vortex characteristics in stable flow, AIChE J. **24**, 869 (1978).
[37] K. Chiba, T. Sakatani, and K. Nakamura, Anomalous flow patterns in viscoelastic entry flow through a planar contraction, J. Non-Newtonian Fluid Mech. **36**, 193 (1990).
[38] K. Chiba, S. Tanaka, and K. Nakamura, The structure of anomalous entry flow patterns through a planar contraction, J. Non-Newtonian Fluid Mech. **42**, 315 (1992).
[39] J. P. Rothstein and G. H. McKinley, The axisymmetric contraction–expansion: The role of extensional rheology on vortex growth dynamics and the enhanced pressure drop, J. Non-Newtonian Fluid Mech. **98**, 33 (2001).
[40] D. V. Boger and R. J. Binnington, Experimental removal of the re-entrant corner singularity in tubular entry flows, J. Rheol. **38**, 333 (1994).
[41] C. Chmielewski, K. L. Nichols, and K. Jayaraman, A comparison of the drag coefficients of spheres translating in corn-syrup-based and polybutene-based boger fluids, J. Non-Newtonian Fluid Mech. **35**, 37 (1990).
[42] M. J. Solomon and S. J. Muller, Flow past a sphere in polystyrene-based Boger fluids: The effect on the drag coefficient of finite extensibility, solvent quality and polymer molecular weight, J. Non-Newtonian Fluid Mech. **62**, 81 (1996).
[43] L. E. Rodd, D. Lee, K. H. Ahn, and J. J. Cooper-White, The importance of downstream events in microfluidic viscoelastic entry flows: Consequences of increasing the constriction length, J. Non-Newtonian Fluid Mech. **165**, 1189 (2010).
[44] M. K. Raihan, S. Wu, Y. Song, and X. Xuan, Constriction length dependent instabilities in the microfluidic entry flow of polymer solutions, Soft Matter **17**, 9198 (2021).
[45] Z. Li, X.-F. Yuan, S. J. Haward, J. A. Odell, and S. Yeates, Non-linear dynamics of semi-dilute polydisperse polymer solutions in microfluidics: A study of a benchmark flow problem, J. Non-Newtonian Fluid Mech. **166**, 951 (2011).
[46] F. Khalkhal, K. H. Chaney, and S. J. Muller, Optimization and application of dry film photoresist for rapid fabrication of high-aspect-ratio microfluidic devices, Microfluid. Nanofluid. **20**, 153 (2016).
[47] A. Nussinovitch, *Hydrocolloid Applications Gum Technology in the Food and Other Industries* (Blackie Academic & Professional, London, 1997).
[48] Xanthan gum, https://www.cpkelco.com/products/xanthan-gum/.
[49] L. B. Smolka and A. Belmonte, Charge screening effects on filament dynamics in xanthan gum solutions, J. Non-Newtonian Fluid Mech. **137**, 103 (2006).
[50] POLYOX water-soluble resins (NF grades), https://www.americanpharmaceuticalreview.com/25260-Excipients/5821954-POLYOX-NF-Grade-Water-Soluble-Resin/.

[51] P. J. Whitcomb and C. W. Macosko, Rheology of xanthan gum, J. Rheol. **22**, 493 (1978).
[52] M. Milas and M. Rinaudo, Properties of xanthan gum in aqueous solutions: Role of the conformational transition, Carbohydr. Res. **158**, 191 (1986).
[53] L. H. Sperling, *Introduction to Physical Polymer Science*, 4th ed. (Wiley-Interscience, Hoboken, NJ, 2005).
[54] N. Burshtein, K. Zografos, A. Q. Shen, R. J. Poole, and S. J. Haward, Inertioelastic Flow Instability at a Stagnation Point, Phys. Rev. X **7**, 041039 (2017).
[55] W. W. Graessley, Polymer chain dimensions and the dependence of viscoelastic properties on concentration, molecular weight and solvent power, Polymer **21**, 258 (1980).
[56] K.-W. Song, Y.-S. Kim, and G.-S. Chang, Rheology of concentrated xanthan gum solutions: Steady shear flow behavior, Fibers Polym. **7**, 129 (2006).
[57] L. Zhong, M. Oostrom, M. J. Truex, V. R. Vermeul, and J. E. Szecsody, Rheological behavior of xanthan gum solution related to shear thinning fluid delivery for subsurface remediation, J. Hazard. Mater. **244–245**, 160 (2013).
[58] M. Chinaud, T. Delaunay, S. Cazin, E. Cid, and Ph. Tordjeman, Milli-PIV rheology of shear-thinning fluids, J. Non-Newtonian Fluid Mech. **169–170**, 114 (2012).
[59] M. Y. Hwang, H. Mohammadigoushki, and S. J. Muller, Flow of viscoelastic fluids around a sharp microfluidic bend: Role of wormlike micellar structure, Phys. Rev. Fluids **2**, 043303 (2017).
[60] S. Gulati, C. S. Dutcher, D. Liepmann, and S. J. Muller, Elastic secondary flows in sharp 90 degree micro-bends: A comparison of PEO and DNA solutions, J. Rheol. **54**, 375 (2010).
[61] S. J. Haward, A. Jaishankar, M. S. N. Oliveira, M. A. Alves, and G. H. McKinley, Extensional flow of hyaluronic acid solutions in an optimized microfluidic cross-slot device, Biomicrofluidics **7**, 044108 (2013).